Supplementary: End-to-end Optimization of Fluidic Lenses

MULUN NA*, HÉCTOR A. JIMÉNEZ-ROMERO*, XINGE YANG, JONATHAN KLEIN, DOMINIK L. MICHELS, and WOLFGANG HEIDRICH, KAUST, KSA

A SUPPLEMENTARY MATERIAL

This document contains additional information and descriptions to our main paper.

A.1 Shift Invariance of the ODE Solution

We prove that the solution h of the system ODE:

$$\begin{cases} h_{rr} = (\rho^* \cdot h + p^*)(1 + h_r^2)^{\frac{3}{2}} - \frac{h_r(1+h_r^2)}{r}, \\ h(R_0) = h_0, \\ h_r(0) = 0. \end{cases} \tag{1}$$

is shift-invariant. A simple translation of $h(r)$ can be defined as $H(r) = h(r) - d$. We also know that the shifted solution $H(r)$ satisfies

$$\begin{cases} h(r) = H(r) + d, \\ h_r = H_r, \\ h_{rr} = H_{rr}. \end{cases}$$

By substitution into Eq. (1), we can obtain a set of parameter ρ_H^* and p_H^* for the shifted result $H(r)$ that can also satisfy the ODE:

$$H_{rr} = (\rho^* \cdot H + \rho^* \cdot d + p^*)(1 + H_r^2)^{\frac{3}{2}} - \frac{H_r(1 + H_r^2)}{r}, \tag{2}$$

where $\rho_H^* = \rho^*$ and $p_H^* = p^* + \rho^* \cdot d$. The problem becomes an initial value problem (**IVP**) when $H(0) = 0$ and we call $d = h_c$ center thickness:

$$\begin{cases} H_{rr} = (\rho_H^* \cdot H + p_H^*)(1 + H_r^2)^{\frac{3}{2}} - \frac{H_r(1+H_r^2)}{r}, \\ H(0) = 0, \\ H'(0) = 0. \end{cases} \tag{3}$$

This means, that we can use a numerical solver to solve the modified **IVP** first and then shift the solution by h_c to obtain the actual surface function.

A.2 Parameter Units

The units of the parameters are provided in Table 1.

Table 1. Overview of parameter units.

Name	Symbol	Physical Unit
Density	ρ	g/cm^3
Volume	V	ml
Surface tension	γ	mN/m
Surface parameter (volume)	p^*	m/mN
Surface parameter (buoyancy)	ρ^*	1 /mm^2
Center thickness	h_c	mm
Ring height	h_0	mm
Lens radius	R_0	mm
Surface solutions	$h(r)$	mm

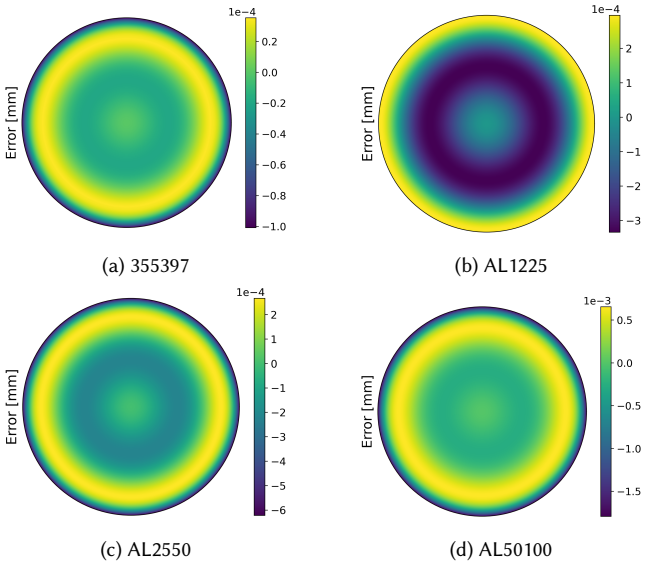

(a) 355397 (b) AL1225 (c) AL2550 (d) AL50100

Fig. 1. Geometrical fitting of aspherical surfaces.

A.3 Geometrical Fitting of Aspherical Lenses

To evaluate the expressiveness of our parameter space, we find optimal fits of four commercially available lenses. Their shapes are defined through the parameters of the aspherical surface model, see Table 2. We find the closest correspondence of each lens in our fluidic design space, the parameters are given in Table 3. The comparison of the surface is shown in Fig. 1.

A.4 Numerical Evaluation Results

The exact values for the bar plots from Fig.7 in the main manuscript are given in Table 4.

*Authors contributed equally to this work.

SA Conference Papers '24, December 3–6, 2024, Tokyo, Japan

ACM ISBN 979-8-4007-1131-2/24/12.
https://doi.org/10.1145/3680528.3687584

Table 2. Parameters for different common lenses.

Parameter \ Lens	355397	AL1225	AL2550	AL50100
R_0 [mm]	3.6	6.25	12.5	25.0
c^{-1} [mm]	-8.789661	12.78	25.56	51.12
κ	-0.905894	-0.6	-1.01	-0.575
$\alpha_4[\text{mm}^{-3}]$	$-3.790758E-05$	$1.8429898E-06$	$3.2703958E-06$	$-4.8366264E-11$
α_6 [mm^{-5}]	$1.563752E-07$	$-3.8172252E-09$	$7.7205335E-10$	$-8.5756915E-12$
α_8 [mm^{-7}]		$-2.4345457E-11$	$1.6304727E-13$	$-2.0138223E-15$
α_{10} [mm^{-9}]		$3.1730496E-14$		$-4.5977971E-19$
α_{12} [mm^{-11}]		$-3.70023E-15$		
α_{14} [mm^{-13}]		$6.5107821E-17$		
α_{16} [mm^{-15}]		$-4.9604147E-19$		

Table 3. Surface parameters fits for the fluidic lens design space for different common lenses. The center thickness h_c is ignored for comparison.

Parameter \ Compared Lens	355397	AL1225	AL2550	AL50100
ρ^*	$-2.2745834E-01$	$-1.5636292E-01$	$-3.2094405E-03$	$-8.0497056E-04$
p^*	$-3.4536123E-02$	$-1.2754912E-02$	$-7.8180819E-02$	$-3.9090216E-02$

Table 4. Numerical values for bar plots from Fig.7 of the main manuscript.

	PSNR			SSIM		
	Plano-Convex	Biconvex	Triplet	Plano-Convex	Biconvex	Triplet
Stock Sensor	22.408	22.1451	23.6516	0.5998	0.5693	0.634
Fluidic Sensor	21.9669	22.6693	23.964	0.5853	0.6379	0.6832
Stock Reconstruction	34.8489	29.7226	29.6746	0.9637	0.9039	0.9193
Fluidic Reconstruction	34.7655	34.8416	35.967	0.9627	0.9612	0.9706

Table 5. Parameters for end-to-end optimized Plano-Convex, Biconvex, and Triplet lenses.

Parameter	Plano-Convex	Biconvex		Triplet					
Surface	1	1	2	1	2	3	4	5	6
h_c	5.9568038E+00	3.7109742E+00	3.6878038E+00	1.5067747E+00	1.7522398E+00	5.2045500E-01	1.7846786E+00	2.3479042E+00	1.2591406E+00
p^*	-7.7884770E-02	-6.8167750E-02	-1.1736010E-02	-9.0246190E-02	-8.9550100E-03	7.0978950E-02	7.1976420E-02	-2.6245880E-02	-9.9663560E-02
ρ^*	-3.4842600E-03	-3.5050400E-03	2.1354500E-03	-1.5056140E-02	-3.0823020E-02	-3.5078410E-02	-5.0395090E-02	-3.1926090E-02	-3.2503200E-02

A.5 Properties of involved liquids

For the experimental realization, we characterized the relevant properties of the liquids involved in the study, as summarized in Table 6. Liquid densities were measured using a density meter (Anton Paar, model DMA 4500 M). The wavelength-dependent refractive index of the optical resin, represented by its dispersion curve, was determined using a spectroscopic ellipsometer (J.A. Woollam, model M-2000) and fitted to a standard Cauchy model. This refractive index model is essential for the end-to-end optimization process accuracy. The average interfacial tension between the glycerol-water solution and the optical resin was measured using an optical tensiometer (Biolin Scientific, model Theta) through pendant drop experiments. Finally, initial estimations of resin shrinkage due to the curing process were obtained using the optical tensiometer by tracking the drop volume change under a fixed dose of 507 mJ/cm^2 of UV light, with a primary peak at 405 nm and a secondary peak at 365 nm, for various intensities.

A.6 Measurement of Curvature Radius

The curvature radius $R = 1/c$ of the manufactured lenses was measured to assess the repeatability of our fabrication method. First, we captured digital images of the lens profile using an optical tensiometer (Biolin Scientific, model Theta), where each pixel corresponds to a length of approximately 14 μm. To estimate the curvature radius, we applied a standard edge detection algorithm followed by a least-squares curve-fitting procedure. Two distinct approaches were employed for curve fitting: one using a spherical description and the other using an aspherical expansion truncated at the fourth-order coefficient, A_4, to address numerical instability. The equations governing these descriptions are detailed in the main text. Fig. 3 illustrates this process, including the type of images acquired, the curvature sampling, and the corresponding fitted curve. One limitation of this method is the maximum clear aperture size that the equipment can measure, which is approximately 16 mm, whereas the lenses used in this study have a diameter of 20 mm.

Table 6. Summary of the physical properties measured for our prototypes fabrication.

Physical quantity	Value
Water density [g/ml, 21°C]	0.99790
Glycerol density [g/ml, 21°C]	1.25980
Resin density [g/ml, 21°C]	1.07983
Resin refractive index	$n(\lambda) = 1.5028 + \frac{5765.82}{\lambda^2}$
Resin volumetric shrinkage [%]	4.6
Average interfacial tension between glycerol-water solution and resin [mN/m]	7.69

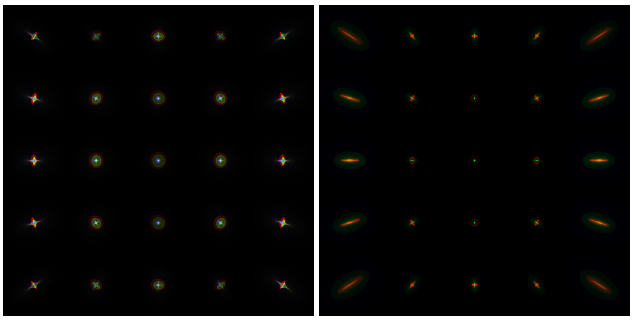

Fig. 2. Top right quadrant PSF map of stock and fluidic lenses. The stock lens (left) is designed to optimize the RMS spot size, which is agnostic to imaging quality. Consequently, despite the PSF exhibiting a small size, the final reconstructed images may lack sharpness. In contrast, the fluidic lens (right), optimized for image loss and jointly with a reconstruction network, aims to achieve the best output image quality. As a result, although the PSF spreads over a larger region, the simulated images can be well reconstructed by the network.

Results for several prototypes analyzed using each method are summarized in Table 7. Due to the inherent limitations of this method, only the most highly curved surface of each lens was included in the analysis. The deviations from the expected values ranged approximately ±8%. Despite this relatively small uncertainty, considering the current lack of automation, there is potential for improvement in the manufacturing process. Some of this enhancements are discussed further in Section A.7.

A.7 Issues of the Manufacturing Process

The imaging results of our manufactured lenses do not quite match the expected results from our simulations which we attribute to the prototype stage of our manufacturing process. Most of the current issues can be traced back to the need for a more controlled fabrication process with tighter controls over the various parameters. This should not be surprising for a relatively new fabrication method like fluidic shaping, and we believe that all these issues can be addressed in the future:

1) Since the photo-polymer and the immersion liquid are not perfectly immiscible, the interfacial tension γ between them will vary over time. As an initial step, we conducted precise interfacial tension measurements across various glycerol concentrations using an optical tensiometer. This method involves capturing the image of a liquid droplet, which is immersed in a second liquid and suspended from the tip of a needle. The droplet's contour is extracted and

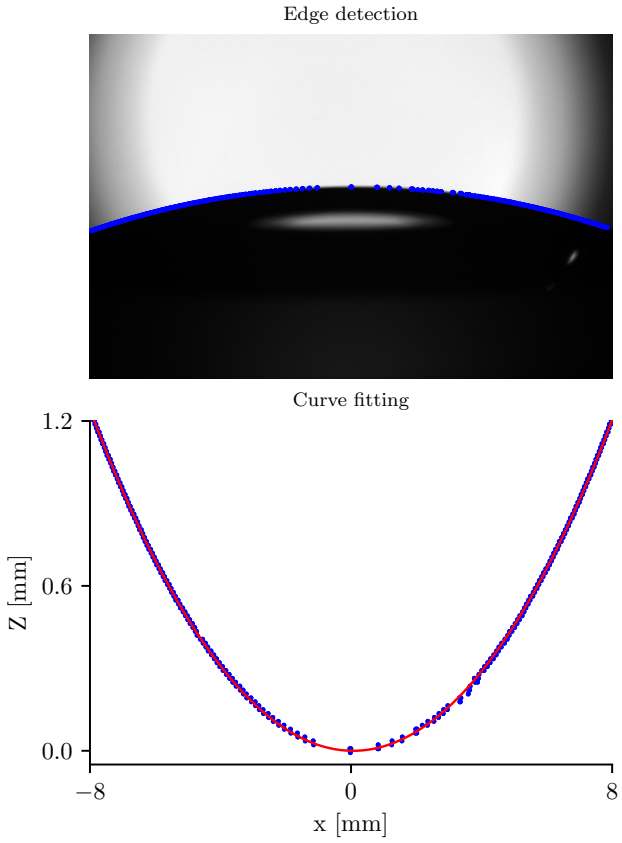

Fig. 3. Example of curve fitting process to determine the best-fit curvature radius. The data points displayed were extracted from the digital image and subsequently fitted to a curve using a least-squares method.

subsequently fitted to a solution of the Young-Laplace equation, enabling the determination of the interfacial tension. An example of such measurement is shown in Fig. 4. Each measured interfacial tension is averaged over time for at least three drops. We estimate the uncertainty in γ at around 1 %, which is roughly comparable (for typical lens sizes) to a volume error of the same magnitude.

2) The rings holding the lens resin are printed using a Formlabs 3D printer. When measuring the results, we found diameter discrepancies of up to 50 μm and height discrepancies of up to 90 μm. These amount to volume changes of up to 2.5 % and impact directly on the

Table 7. Curvature radius estimation is performed using both spherical and aspherical models to fit the optimal curve. The errors are calculated relative to the expected design values. For the AL2550-GEO model, the anticipated curvature radius is $R = 25.56$ mm, whereas for the LBF254-050-E2E model, the expected curvature radius is $R = 30.52$ mm.

Prototype code	Aspheric curve fitting			Spheric curve fitting		
	MSE	R [mm]	Err R [%]	MSE	R [mm]	Err R [%]
AL2550-GEO-2	0.411	27.519	7.66	0.441	26.854	5.06
AL2550-GEO-3	0.197	25.446	-0.45	0.223	24.931	-2.46
AL2550-GEO-7	0.274	24.958	-2.36	0.295	25.396	-0.64
LBF254-050-E2E-2	0.413	30.041	-1.57	0.426	30.532	0.04
LBF254-050-E2E-3	0.216	28.25	-7.44	0.315	29.488	-3.38
LBF254-050-E2E-4	0.421	28.976	-5.06	0.422	29.056	-4.80

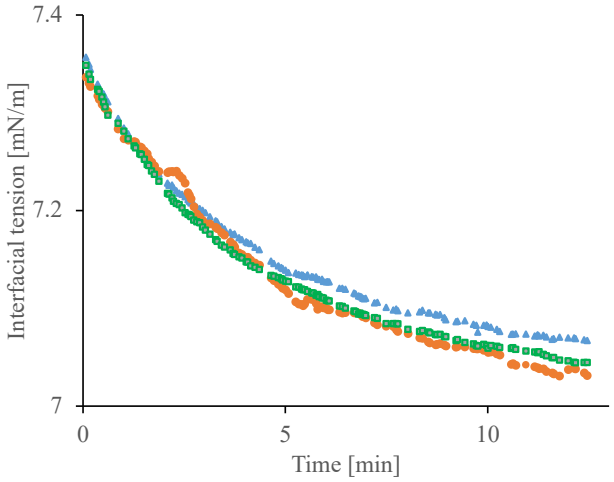

Fig. 4. Variation of interfacial tension over time is presented. Each data set corresponds to distinct drops of UV resin immersed in a solution of water and glycerol, all subjected to identical initial conditions.

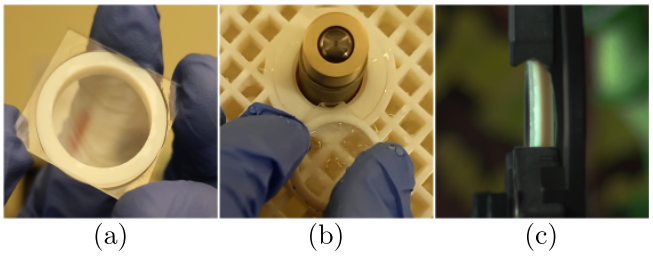

Fig. 5. Illustration of the modified fabrication method for lenses requiring a flat side. In (a), the attachment of the lens frame to the glass microscope slide is depicted. In (b), the removal of excess material is shown. Finally, in (c), the completed prototype, including the glass layer, is presented.

curved surface shape. While the injected volume can be adjusted accordingly, and the error in curvature is thus greatly reduced, the lens height will still be off. In principle, more advanced 3D printers are already available and could be employed to mitigate these problems.

3) The injection syringe has a threaded plunger that releases a volume of 13.23 μl per turn, where the smallest controllable amount is half of a turn. For typical lens volumes, this corresponds to an error of roughly 0.5 %. Switching to fully automatic injection devices, a higher precision could be achieved.

4) The photo-polymer curing is a complex and highly sensitive process. Depending on the specific polymer the shrinkage can be up to 14 %. For the polymer used in this paper (Vida Rosa, 2nd generation), we conducted a series of experiments on individual drops and found, that the volume initially raised between 1 % and 10 % (depending on illumination strength), before slowly converging to an overall volume reduction of around 4.6 %, mostly independent of the illumination strength. This is not the only aspect of the curing process that we have considered. We have also observed that utilizing LED UV light sources to cure our samples results in distinct interference-like patterns on the lens surface. To address these artifacts that may impact the imaging process, we have implemented a quartz diffuser between the lens and the UV lamp. Still, different parts of the lens will inherently cure at different points in time, leading to complex shape deformations. Future research should investigate these deformations in more detail. For example, an accurate shrinkage model could be used to precisely counteract the effect in an inverse simulation fashion.

5) For lenses requiring a flat side, as described in the main paper, a polycarbonate sheet was initially employed in our prototypes primarily because it is easily detachable from the lens body. However, the flexibility of the polycarbonate sheet poses a significant drawback, as it cannot guarantee the flatness required for most optical applications. To address this issue, we introduced a minor modification in the plano-convex lens manufacturing process during the submission of this report. Specifically, we replaced the polycarbonate sheet with a glass microscope slide to produce the flat side of the lens, which was then left attached to the final prototype. The excess material was subsequently ground away, as illustrated in Fig. 5.

This adjustment resulted in improved optical performance, allowing us to capture higher-quality raw images. As usual, these images are then post-processed using the jointly optimized network to achieve optimal results.

In Fig. 6, we present preliminary findings that strongly suggest integrating this modification into the manufacturing process. It is crucial to note that the computational models must also account for this additional optical element to ensure optimal performance.

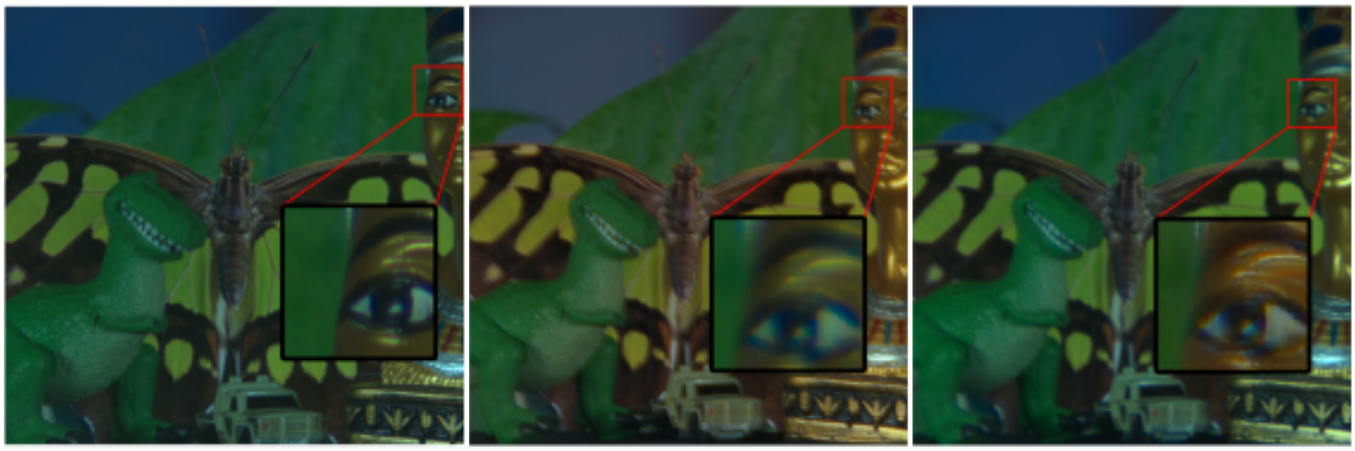

Fig. 6. Preliminary results demonstrate the positive impact on image capturing and reconstruction after adding a microscope glass slide to the back of the plano-convex lens. From left to right: (a) ground truth captured with the Thorlabs plano-convex lens AL-2550, (b) raw image taken with our manufactured prototype, code AL-2550-GEO-7, and (c) reconstructed image produced by the jointly trained network.

Furthermore, these initial results indicate the necessity for further assessments to fully validate the effectiveness of this modification.

Despite the challenges of the manufacturing process, we strongly believe that fluidic shaping has a promising future in prototyping and small volume production of optical elements. Particularly the ability to create both spherical and aspherical surfaces with no extra cost is highly attractive. Our work bridges the design gap for this exciting new fabrication method, as such we believe it significantly advances the viability of this approach.